Experimental assessment of the similarity laws for two-dimensional nonlinear heat transfer in building material

Julien Berger, Clemence Legros

Experimental assessment of the similarity laws for two-dimensional non-linear heat transfer in building material

Julien Berger [a*], Clemence Legros[b,c]

November 8, 2022

[a] Laboratoire des Sciences de l'Ingénieur pour l'Environnement (LaSIE), UMR 7356 CNRS, La Rochelle Université, CNRS, 17000, La Rochelle, France
[b] Univ. Savoie Mont Blanc, CNRS, LOCIE, 73000 Chambéry, France
[c] Univ. Grenoble Alpes, CEA, LITEN, DTS, INES, 38000 Grenoble, France
*corresponding author, e-mail address : julien.berger@univ-lr.fr

Abstract

Based on the dimensionless formulation of the problem, the similarity laws are a very powerful tool to scale up or down configurations of heat conduction transfer. It enables to define equivalent configurations according to a proportionality ratio. If the latter is lower than 1 , the equivalent configuration has reduced scales. Indeed, the characteristic time of the equivalent configuration is reduced by the square of ratio of the characteristic lengths. In this article, the reliability of the similarity laws are investigated to define equivalent configurations in terms of kinetics of nonlinear two-dimensional heat transfer process in a building porous material. For this, experimental observations are generated for a woodfiber material submitted to a dynamic thermal stress in a climatic chamber. Then, the top and lateral surfaces heat transfer coefficients are determined using an inverse problem approach. Once the whole problem parameters known, equivalent numerical configurations are defined based on the similarity laws. Experimental results and numerical predictions are compared. It highlights a satisfactory agreement between both, with discrepancies remaining within the range of the observation uncertainties. Those results validates the use of similarity laws for defining equivalent configurations of the considered problem of heat transfer.

Key words: similarity analysis; dimensionless number; heat transfer; model reliability; experimental results;

1 Introduction

The modeling of building energy efficiency is of primary importance since the first oil crisis. Several building energy model have been elaborated to assess accurately the heat losses through building walls considering both sensible and latent heat transfer. A recent review of the developed models have been proposed in [1].

The accuracy of the model predictions requires to be evaluated through a fine comparison with experimental observations. It enables to estimate the model reliability and verify the physical hypothesis. Several works in the literature proposed experimental observations of the physical phenomena to benchmark the numerical models. A extensive review is proposed in [2]. An example may be consulted in [3]. For building construction material, the characteristic time of heat transfer scales with a few minutes. However the time scales of observations range with one year to evaluate the energy consumption. It can rise to several year when investigating climate change effects [4]. Thus, the acquisition of experimental observation for such time scales is a time-consuming, expensive and challenging issue [5]. Elaborating a reduced-scale experiment enables to tackle those difficulties.

The similarity laws of heat transfer can be a powerful tool to design small scale experiments without loosing kinetics of the physical phenomena. Such laws are based on a dimensionless formulation of the transfer equations. They permit to define equivalencies between physical system regarding the phenomena. As remarked in [6], there is an extensive use of those laws in fields such as fluid dynamics or chemical engineering. For the area of transfer in building porous materials, two recent articles treat of dimensionless formulation of heat and mass transfer equations. In [7], the processes are discussed for a fiberboard material

according to the dimensionless numbers. In [8], the similarity laws are investigated according to kinetic, geometric or transfer dynamics. However, those works only deal with numerical investigations. Note that an early work proposed by MATSUMOTO and FUJIWARA [5] proposed a comparison between reduced scaled experimental results and numerical model predictions. For this work, the boundary conditions are not fully controlled experimentally and defined for the surface transfer coefficients.

This article intends to continue this research line. The aim is to assess the validity of the kinetics similarity of nonlinear two-dimensional heat transfer by comparing the experimental results to the numerical model predictions obtained for an equivalent configuration. Two sets of experimental observations are generated for a woodfiber material placed in a climatic chamber. To improve the work of [5], the heat transfer coefficients are determined using a inverse problem algorithm. Then, the model predictions are compared against the experimental results to investigate the reliability of the similarity laws. The article is structured as follows. Section 2 presents the mathematical model of non-linear heat transfer. Then, Section 3 defines the similarity laws for the problem under investigation. The material and experimental design are described in Section 4. Results and discussion of the thermal similarity reliability are given in Section 5.

2 Formulation of the mathematical model

The heat transfer process occurs in a material placed in a climatic chamber as illustrated in Figure 1. The material is initially at $T_\mathrm{i}\ [\mathsf{K}]$ and then submitted to variations of ambient air T_∞. The temperature T in the material varies over the time horizon $\Omega_t \overset{\text{def}}{:=} [\,0\,,\,t_0\,]\ [\mathsf{s}]$ being the final time. The material is placed in a mold of insulation as illustrated in Figure 1. The temperature depends on the coordinates $(\,x\,,\,y\,) \in \Omega_x \times \Omega_y$ where:

$$\Omega_x \overset{\text{def}}{:=} [\,0\,,\,L_{0,x}\,]\,, \qquad \Omega_y \overset{\text{def}}{:=} [\,0\,,\,L_{0,y}\,]\,,$$

with $L_{0,x}\ [\mathsf{m}]$ and $L_{0,y}\ [\mathsf{m}]$ are the length and width of the material. The two-dimensional governing equations of heat transfer is:

$$c \cdot \frac{\partial T}{\partial t} \;=\; \frac{\partial}{\partial x}\left(k(T)\cdot\frac{\partial T}{\partial x}\right) \;+\; \frac{\partial}{\partial y}\left(k(T)\cdot\frac{\partial T}{\partial y}\right). \tag{1}$$

The material has a volumetric capacity $c\ [\mathsf{W}\,.\,\mathsf{m}^{-3}\,.\,\mathsf{K}^{-1}]$ and a temperature dependent thermal conductivity $k\ [\mathsf{W}\,.\,\mathsf{m}^{-1}\,.\,\mathsf{K}^{-1}]$:

$$k(T) \;=\; k_0 \;+\; k_1 \cdot \frac{T}{T_0}\,. \tag{2}$$

For the boundary conditions, the following interfaces are defined:

$$\Gamma_T \overset{\text{def}}{:=} \{\,x \;=\; 0\,|\,y \in \Omega_y\,\}\,, \qquad \Gamma_B \overset{\text{def}}{:=} \{\,x \;=\; L_{0,x}\,|\,y \in \Omega_y\,\}\,,$$
$$\Gamma_L \overset{\text{def}}{:=} \{\,y \;=\; 0\,|\,x \in \Omega_x\,\}\,, \qquad \Gamma_R \overset{\text{def}}{:=} \{\,y \;=\; L_{0,y}\,|\,x \in \Omega_x\,\}\,.$$

At the top and lateral sides, ROBIN boundary condition are defined to represent the convective transfers occurring:

$$k(T)\cdot\frac{\partial T}{\partial x} \;=\; h_t\cdot\Big(T \;-\; T_\infty(t)\Big)\,, \qquad \forall\,(\,x\,,\,y\,) \in \Gamma_T\,, \tag{3a}$$

$$k(T)\cdot\frac{\partial T}{\partial y} \;=\; h_\ell\cdot\Big(T \;-\; T_\infty(t)\Big)\,, \qquad \forall\,(\,x\,,\,y\,) \in \Gamma_L\,, \tag{3b}$$

$$k(T)\cdot\frac{\partial T}{\partial y} \;=\; -\,h_\ell\cdot\Big(T \;-\; T_\infty(t)\Big)\,, \qquad \forall\,(\,x\,,\,y\,) \in \Gamma_R\,, \tag{3c}$$

with h_t $\left[\mathsf{W}\,.\,\mathsf{m}^{-2}\,.\,\mathsf{K}^{-1}\right]$ and h_ℓ the top and lateral surface heat transfer coefficients, respectively. At the bottom, due to the insulator, the heat flux is almost null so that homogeneous NEUMANN boundary conditions is written:

$$\frac{\partial T}{\partial x} \;=\; 0\,, \qquad \forall\,(x\,,\,y) \in \Gamma_B\,. \tag{4}$$

At initial condition, the material is in equilibrium at a given temperature T_i:

$$T \;=\; T_\mathrm{i}\,, \qquad \forall (x\,,\,y) \in \Omega_x \times \Omega_y\,, \qquad t \;=\; 0\,.$$

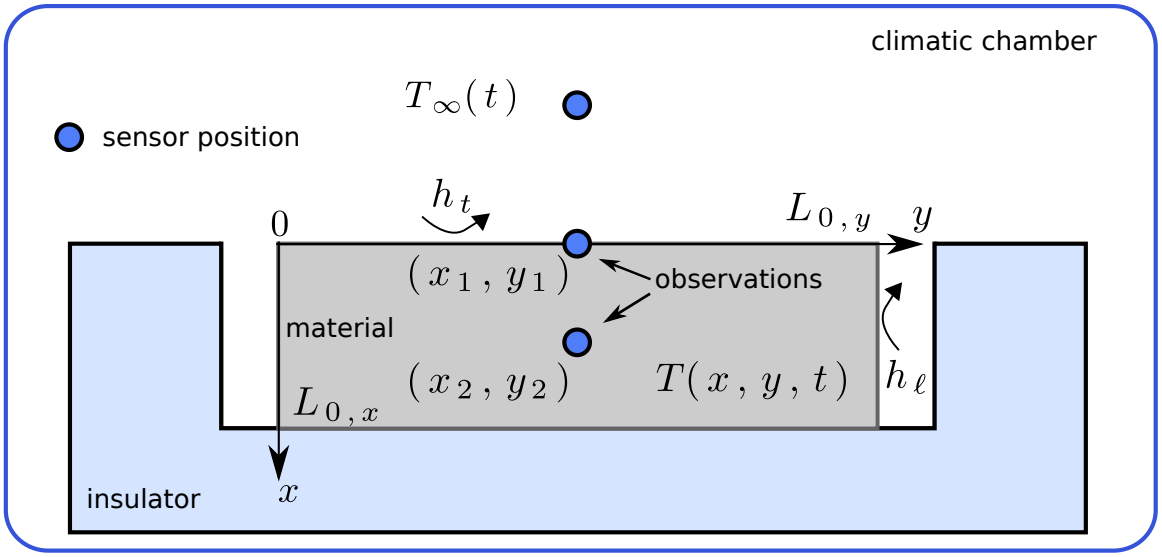

Figure 1. *Illustration of the domain.*

3 Similarity of heat transfer

The similarity of heat transfer starts first with a dimensionless formulation of the governing equations.

3.1 Dimensionless formulation

The following transformation is defined:

$$u \,:\, \left[\,0\,,\,1\,\right]^3 \longrightarrow \mathbb{R} \tag{5a}$$

$$(\chi\,,\,\psi\,,\,\tau) \longmapsto \frac{T}{T_0}\,, \tag{5b}$$

with the dimensionless space and time coordinates:

$$\chi \overset{\text{def}}{:=} \frac{x}{L_{0,x}}\,, \qquad \psi \overset{\text{def}}{:=} \frac{y}{L_{0,y}}\,, \qquad \tau \overset{\text{def}}{:=} \frac{t}{t_0}\,.$$

Thus, the dimensionless problem of Eq. (1) is:

$$\frac{\partial u}{\partial \tau} \;=\; \mathrm{Fo}\cdot\frac{\partial}{\partial \chi}\left(\kappa(u)\cdot\frac{\partial u}{\partial \chi}\right) \;+\; \mathrm{Fo}\cdot r^{\,2}\cdot\frac{\partial}{\partial \psi}\left(\kappa(u)\cdot\frac{\partial u}{\partial \psi}\right). \tag{6}$$

Eq. (6) introduces the FOURIER dimensionless number Fo qualifying the ease of heat conduction in the material (in the x direction) and the ratio of length between material length and width:

$$\mathrm{Fo} \overset{\text{def}}{:=} \frac{k_0 \cdot t_0}{c \cdot L_{0,x}^2}, \qquad r \overset{\text{def}}{:=} \frac{L_{0,x}}{L_{0,y}}. \tag{7}$$

The nonlinear distortion of the thermal permeability is given by:

$$\kappa(u) = 1 + \kappa_1 \cdot u, \qquad \kappa_1 \overset{\text{def}}{:=} \frac{k_1}{k_0}$$

The boundary conditions (3) and (4) are transformed into a dimensionless formulation:

$$\kappa(u) \cdot \frac{\partial u}{\partial \chi} = \mathrm{Bi}_t \cdot \Big(u - u_\infty(\tau) \Big), \qquad \forall (\chi, \psi) \in \Gamma_T^\star, \tag{8a}$$

$$\frac{\partial u}{\partial \chi} = 0, \qquad \forall (\chi, \psi) \in \Gamma_B^\star, \tag{8b}$$

$$\kappa(u) \cdot \frac{\partial u}{\partial \psi} = \mathrm{Bi}_\ell \cdot r \cdot \Big(u - u_\infty(\tau) \Big), \qquad \forall (\chi, \psi) \in \Gamma_L^\star, \tag{8c}$$

$$\kappa(u) \cdot \frac{\partial u}{\partial \psi} = -\mathrm{Bi}_\ell \cdot r \cdot \Big(u - u_\infty(\tau) \Big), \qquad \forall (\chi, \psi) \in \Gamma_R^\star, \tag{8d}$$

with the BIOT number qualifying the ratio of transfer between convective and diffusive modes:

$$\mathrm{Bi}_t \overset{\text{def}}{:=} \frac{h_t \cdot L_{0,x}}{k}, \qquad \mathrm{Bi}_\ell \overset{\text{def}}{:=} \frac{h_\ell \cdot L_{0,x}}{k}. \tag{9}$$

Last, the initial condition is:

$$u = u_\mathrm{i}, \qquad \forall (\chi, \psi) \in \big[0, 1\big]^2, \qquad \tau = 0, \qquad u_\mathrm{i} \overset{\text{def}}{:=} \frac{T_\mathrm{i}}{T_0}. \tag{10}$$

3.2 Similarity laws

Several similarity laws can be defined according to the conservation of the characteristic time t_0, the reference length $L_{0,x}$ or the transfer phenomena. The latter is the focus of these investigations. Two configurations of transfer are assumed and denoted with the superscript $\bar{}$ and $\widehat{}$, respectively. The two are equivalent from a point of view of transfer kinetics if their dimensionless numbers are equals. For the given mathematical problem, it leads to the following system of equations:

$$\begin{cases} \overline{\mathrm{Fo}} = \widehat{\mathrm{Fo}}, \\ \overline{\mathrm{Bi}}_\ell = \widehat{\mathrm{Bi}}_\ell, \\ \overline{\mathrm{Bi}}_t = \widehat{\mathrm{Bi}}_t, \\ \overline{r} = \widehat{r} \end{cases}$$

Given Eqs. (7) and (9), it yields to the following system of equations:

$$\begin{cases} \dfrac{\overline{k}_0 \cdot \overline{t}_0}{\overline{c} \cdot \overline{L}_{0,x}^2} = \dfrac{\widehat{k}_0 \cdot \widehat{t}_0}{\widehat{c} \cdot \widehat{L}_{0,x}^2}, \\ \dfrac{\overline{h}_\ell \cdot \overline{L}_{0,x}}{\overline{k}} = \dfrac{\widehat{h}_\ell \cdot \widehat{L}_{0,x}}{\widehat{k}}, \end{cases} \qquad \begin{cases} \dfrac{\overline{h}_t \cdot \overline{L}_{0,x}}{\overline{k}} = \dfrac{\widehat{h}_t \cdot \widehat{L}_{0,x}}{\widehat{k}}, \\ \dfrac{\overline{L}_{0,x}}{\overline{L}_{0,y}} = \dfrac{\widehat{L}_{0,x}}{\widehat{L}_{0,y}}. \end{cases} \tag{11}$$

It is assumed that the material properties between the two configurations are equal:

$$\overline{k}_0 = \widehat{k}_0, \qquad \overline{c} = \widehat{c}, \qquad \overline{\kappa} = \widehat{\kappa}.$$

Thus, system (11) becomes:

$$\widehat{L}_{0,x} = \Pi \cdot \overline{L}_{0,x}, \quad \widehat{L}_{0,y} = \Pi \cdot \overline{L}_{0,y}, \quad \widehat{t}_0 = \Pi^2 \cdot \overline{t}_0, \quad \widehat{h}_\ell = \frac{1}{\Pi} \cdot \overline{h}_\ell, \quad \widehat{h}_t = \frac{1}{\Pi} \cdot \overline{h}_t, \tag{12}$$

where Π is the proportionality factor between the final time and characteristic length of the two configurations. If two configurations verifies Eq. (12), then there are equivalent in terms of transfer kinetics. This results is particularly important to downscale by two orders the time horizon of the experimental investigations when choosing a factor $\Pi < 1$. For instance, dividing by 10 the length of the material of the reference configuration implies that the final time t_0 is divided by 100 in the equivalent configuration. From a mathematical point of view, the similarity laws (12) represent a mapping between two equivalent configurations:

$$\begin{aligned} \mathcal{S} : \left[0, \overline{L}_{0,x}\right] \times \left[0, \overline{L}_{0,y}\right] \times \left[0, \overline{t}_0\right] &\longrightarrow \left[0, \widehat{L}_{0,x}\right] \times \left[0, \widehat{L}_{0,y}\right] \times \left[0, \widehat{t}_0\right] \\ \left(\overline{x}, \overline{y}, \overline{t}\right) &\longmapsto \left(\widehat{x} = \Pi \cdot \overline{x}, \widehat{y} = \Pi \cdot \overline{y}, \widehat{t} = \Pi^2 \cdot \overline{t}\right). \end{aligned}$$

The graph of similarity laws is presented in Figure 2.

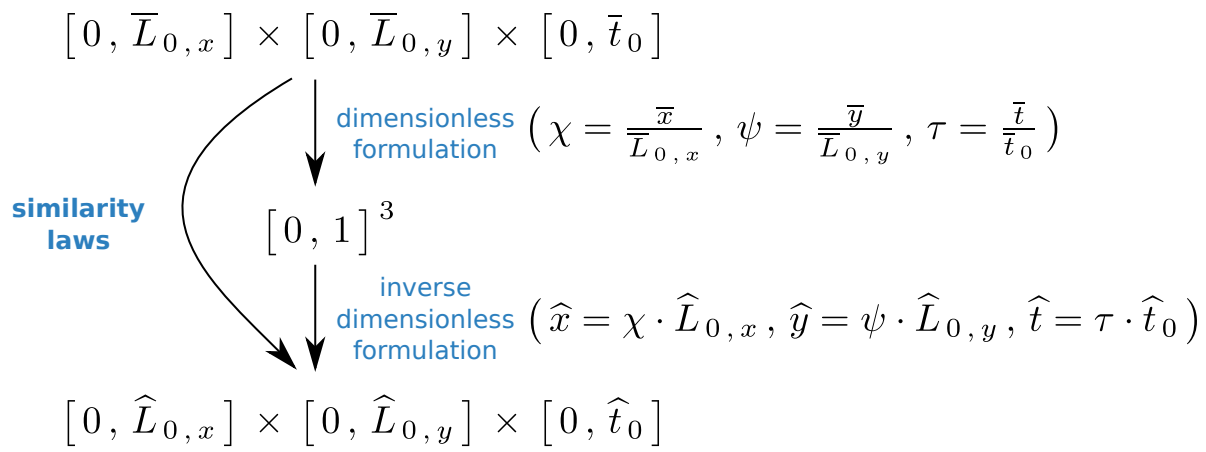

Figure 2. *Graph of the similarity law of the given mathematical problem of heat transfer.*

3.3 Assessing the validity of the similarity laws

To assess the validity of the similarity laws, the following methodology is carried out. First, experimental data are produced using the design described in the next Section. Since, the top and lateral surface transfer coefficients cannot be controlled through the experimental set-up, the second step consists in solving an inverse problem to determine them. For this, the Gauß gradient based algorithm is employed, which description is provided in Appendix A. It requires the solution of the governing and two sensitivity equations. The three partial differential equations are solved using the explicit Du Fort–Frankel numerical model described in Appendix B. It provides an explicit numerical scheme with an extended stability condition. Thus, the computational cost is cut compared to standard approaches. After retrieving the coefficients h_t° and h_ℓ°, the similarity laws are employed to determine an equivalent of the experimental configuration. Last, the a direct simulation using the Du Fort–Frankel scheme is realized to obtain numerical results of the temperature within the equivalent configuration. The latter are compared to the experimental data to evaluate the reliability of the similarity laws. A synthesis of the methodology is presented in Figure 3.

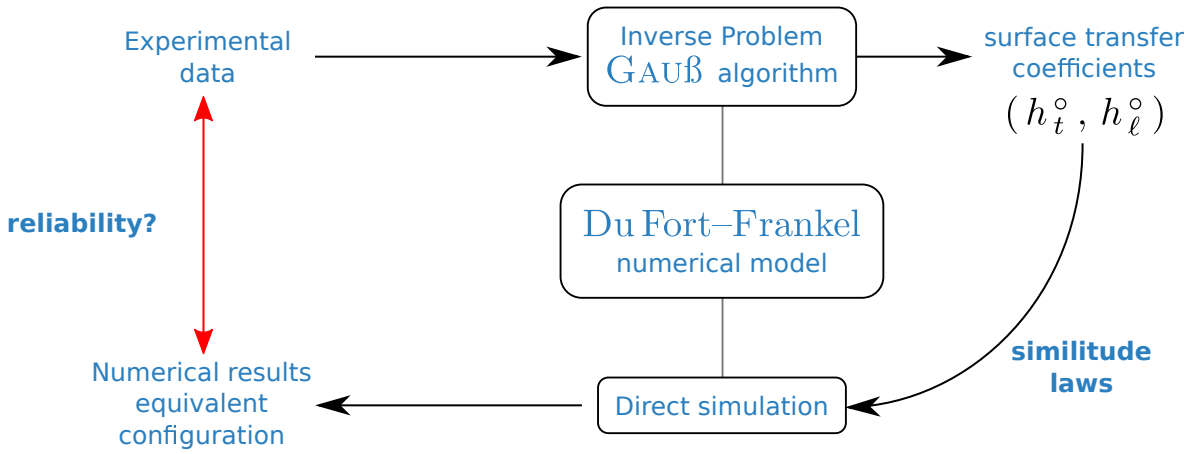

Figure 3. *Illustration of the methodology to assess the reliability of the similarity laws using both experimental data and numerical results.*

4 Experimental design

4.1 Material and methods

To assess the kinetic similarities of heat transfer through an experimental campaign, samples of wood fiber are placed inside a climatic chamber of type `Memmert` ICP 110. The chamber can only control the temperature within the range -12 to $60\ °\mathsf{C}$ with an accuracy of $0.1\ °\mathsf{C}$. The relative humidity is varying freely. The surrounding of the wood fiber are covered with a PU insulator as illustrated in Figures 1 and 4(a). A picture of the samples inside the climatic chamber is given in Figure 4(b). The material properties have been determined in [9]. The coefficients of the thermal conductivity are $k_0 = 8.5{\cdot}10^{-3}\ \mathsf{W.m^{-1}.K^{-1}}$, $k_1 = 3.17{\cdot}10^{-2}\ \mathsf{W.m^{-1}.K^{-1}}$ and $T_0 = 20\ °\mathsf{C}$. The volumetric heat capacity is $c = 1.611{\cdot}10^{5}\ \mathsf{W.m^{-3}.K^{-1}}$.

`Sensirion`$^{\text{TM}}$ SHT75 sensors are placed at the interface between the material and the ambient air, at $x = 0$. To ensure a perfect contact, a thermal paste is used. All sensors have been calibrated in temperature prior to the experiments. The ambient air temperature is recorded twice, by the chamber sensor and by an additional SHT sensor. A sensor is also introduced in the middle of the material. For this, the latter is cut to set the sensor. Then, the material is sealed using an aluminum tape as shown in Figure 4(c).

The chamber is programmed as follows. A first period of 24 h occurs at $20\ °\mathsf{C}$. It ensures to have a homogeneous initial temperature inside the sample. Then, during the first phase, the temperature increases slowly from 20 to $30\ °\mathsf{C}$ at a rate $\mathrm{R}\ [\,°\mathsf{C.s^{-1}}]$ during the time interval $[\,0\,,\,t_a\,]$. The temperature is then maintained at $30\ °\mathsf{C}$ within the time interval $[\,t_a\,,\,t_b\,]$. During the last phase $[\,t_b\,,\,t_0\,]$, the temperature decreases to $20\ °\mathsf{C}$ at a rate $-\mathrm{R}\ [\,°\mathsf{C.s^{-1}}]$. The imposed boundary conditions can be formulated as follow:

$$T_\infty(t) = \begin{cases} 20\ °\mathsf{C}\,, & t < 0\,, \\ \mathrm{R}\cdot t\,, & t \in [\,0\,,\,t_a\,]\,, \\ 30\ °\mathsf{C}\,, & t \in [\,t_a\,,\,t_b\,]\,, \\ -\mathrm{R}\cdot t\,, & t \in [\,t_b\,,\,t_0\,]\,. \end{cases}$$

It is important to note that the surface transfer coefficients h_ℓ and h_t cannot be control through the experimental facility. The chamber ventilator velocity is set to the maximal value. Before evaluating the reliability of the similarity law, a parameter estimation problem is solved to evaluate the transfer coefficient of both experimental configurations. A GAUß algorithm is employed, which description is provided in

Appendix A.

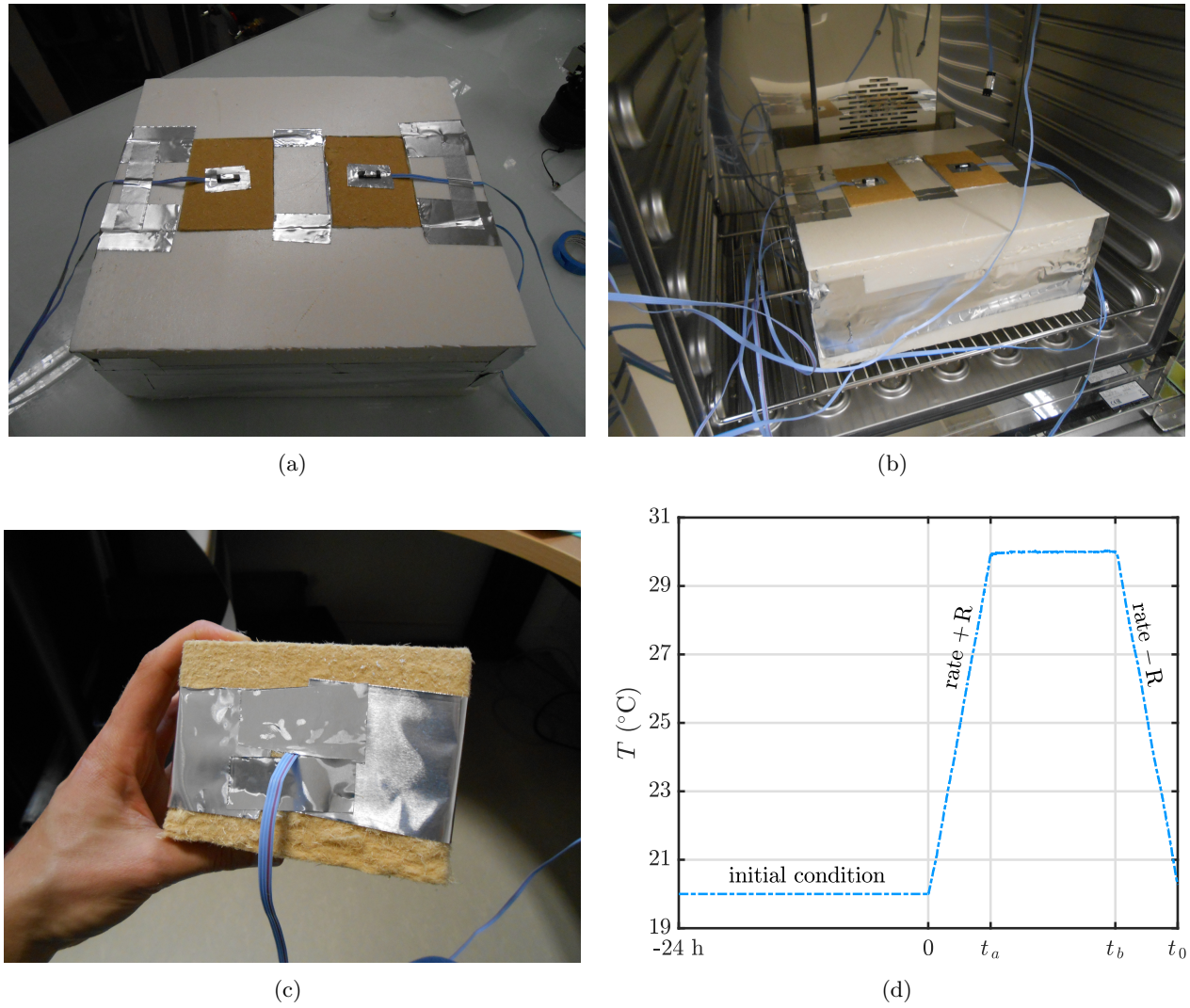

Figure 4. *Illustration of the samples inserted in the insulator* (a)*, in the climatic chamber* (b) *and of the insertion of the sensor at* $x = L_0$*. Time variation of the set-up temperature in the climatic chamber* (d).

4.2 Measurement uncertainties

For each configuration, the campaign is repeated $N_e = 3$ times to decrease the random aspect of the measurement uncertainties. Thus, the best estimates of the temperature measurement in the material is given by [10]

$$T_{\text{exp}}(x_j, y_j, t^n) \overset{\text{def}}{:=} \frac{1}{N_e} \sum_{i=1}^{N_e} \hat{T}_{\text{obs},i}(x_j, y_j, t^n), \qquad j \in \{1, \dots, N_s\}, \qquad n \in \{1, \dots, N_m\},$$

where N_m is the number of time measurement and N_s is the sensors number. The total uncertainty σ [K] of the temperature measurement is evaluated through a complete propagation of each uncertainties:

$$\sigma \overset{\text{def}}{:=} \sqrt{\sigma_s^2 + \sigma_{\sim}^2 + \sigma_x^2},$$

where $\sigma_s = 0.3\ ^\circ\mathsf{C}$ is the sensor measurement uncertainty. The random part $\sigma_\sim$ of the uncertainty:

$$\sigma_\sim \overset{\text{def}}{:=} \frac{1}{\sqrt{N_e}} \sqrt{\frac{1}{N_e} \sum_{i=1}^{N_e} \left(\hat{T}_{\text{obs},i} - T_{\text{exp}}\right)^2}\,.$$

The uncertainty on the sensor position σ_x is evaluated by:

$$\sigma_x \overset{\text{def}}{:=} \frac{\partial T}{\partial x} \cdot \delta_x + \frac{\partial T}{\partial y} \cdot \delta_y\,,$$

where $\delta_x = \delta_y = 5\ \mathsf{mm}$ is the sensor position uncertainty. Both derivatives $\dfrac{\partial T}{\partial x}$ and $\dfrac{\partial T}{\partial y}$ are evaluated using a numerical solution of the governing equation.

5 Results

Two experimental configurations are produced for the investigations as reported in Table 1. The first one considers a material of height $L_{0,x} = 8\ \mathsf{cm}$. The final time of the investigations is $t_0 = 20\ \mathsf{h}$. The second configuration considers a smaller material with $L_{0,x} = 4\ \mathsf{cm}$. The duration of the investigation is also shorter with $t_0 = 5\ \mathsf{h}$. The other parameters of the boundary conditions are given in the corresponding Table.

Table 1. *Main parameters of the two configurations considered for generating experimental observations.*

	Height	*Width*	*Final time*	*Boundary conditions*			*Surface coefficients*	
	$L_{0,x}$	$L_{0,y}$	t_0	R	t_a	t_b	h_t	h_ℓ
Configuration	$[\mathsf{cm}]$	$[\mathsf{cm}]$	$[\mathsf{h}]$	$[^\circ\mathsf{C}.\mathsf{h}^{-1}]$	$[\mathsf{h}]$	$[\mathsf{h}]$	$[\mathsf{W}.\mathsf{m}^{-2}.\mathsf{K}^{-1}]$	$[\mathsf{W}.\mathsf{m}^{-2}.\mathsf{K}^{-1}]$
experimental 1	8	8	20	2	5	15	44.12	2.46
numerical equivalent 1 $\Pi = 0.25$	2	2	1.25	32	0.3125	0.9375	176.48	9.84
experimental 2	4	8	5	8	1.25	3.75	129.44	4.55
numerical equivalent 2 $\Pi = 5$	20	40	125	0.32	31.25	93.75	25.88	0.91

5.1 Configuration 1

Results of the first configuration are now considered. Two sets of experimental observations are obtained using two sensors at $(x_1, y_1) = (0, 4)\ \mathsf{cm}$ and $(x_2, y_2) = (4, 4)\ \mathsf{cm}$, respectively.

To assess the reliability of the heat transfer similarity, the first step is to determine the surface transfer coefficient of the experimental configuration. Note that the theoretical identifiability of the parameters has been verified even if it is not presented in the results. The practical identifiability is verified by analyzing the sensitivity functions shown in Figure 5 and computed with the initial guesses $h_t^1 = 8\ \mathsf{W}.\mathsf{m}^{-2}.\mathsf{K}^{-1}$ and $h_\ell^1 = 0.1\ \mathsf{W}.\mathsf{m}^{-2}.\mathsf{K}^{-1}$. The magnitude of the sensitivity functions varies according to the boundary conditions evolution. As expected, the magnitude of the function φ, corresponding to the coefficient h_ℓ^1, is lower for the sensor located at the top surface. Indeed, this coefficient impacts the lateral boundary surfaces. The correlation coefficient between the functions is 0.45 indicating no linear dependency. Thus, the two unknown parameters can be estimated with the inverse algorithm.

The Gauss algorithm is used considering convergence tolerances set to $\text{Tol}_1 = \text{Tol}_2 = 10^{-5}$. The discretisation parameter of the numerical model are fixed to $\Delta x = \Delta y = 10^{-2}$ and $\Delta t = 10^{-3}$ (in dimensionless formulation). The evolution of the estimated parameters are presented in Figures 6(a) and 6(b). In

addition, the variation of the convergence criteria are shown in Figure 6(c). After 14 iterations, the algorithm converged and the estimated parameters are $h_t^\circ = 44.12\ \mathsf{W.m^{-2}.K^{-1}}$ and $h_\ell^\circ = 2.46\ \mathsf{W.m^{-2}.K^{-1}}$. Results are also reported in Table 1. As expected, the top surface transfer coefficients is higher than the lateral one. Indeed, the top surface is more exposed to the airflow of the chamber ventilator. To check the robustness of the estimated parameters, the algorithm is run for four different initial guesses spread in the parameter space. Results are illustrated in Figure 6(d). It can be remarked that the four runs converge to the same estimates, validating the obtained results.

The second step consists in running the direct model for an equivalent configuration to the experimental one, according to the similarity laws. The numerical equivalent configuration is defined for a proportionality ratio $\Pi = 0.25$. The corresponding parameters of the equivalent configuration are evaluated and reported in Table 1. Since the proportionality ratio is lower than 1, the characteristic time and space are reduced. Figure 7 shows a comparison between the experimental results and the model prediction of both configurations. The observation uncertainties are reported with the grey shadow. A very good agreement is observed between the results. The residual remains mostly in the range of the measurement uncertainties. Those results validate the reliability of the similarity laws of heat transfer for this configuration.

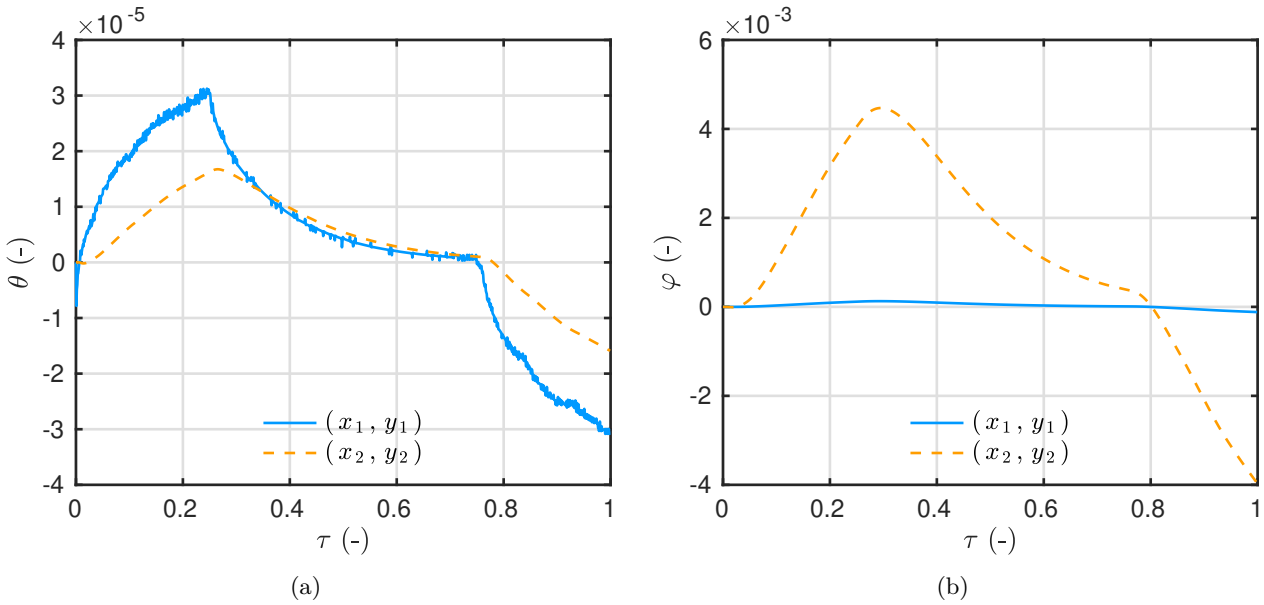

Figure 5. *Variation of the sensitivity function of the coefficients* h_t (a) *and* h_ℓ (b) *computed with the initial guesses.*

5.2 Configuration 2

The configuration 2 is now investigated to evaluate the accuracy of the similarity laws. As for the previous case, two sensors are placed at the top surface and in the middle of the material: $(x_1, y_1) = (0, 4)\ \mathsf{cm}$ and $(x_2, y_2) = (2, 4)\ \mathsf{cm}$.

Before solving the inverse problem, the identifiability of the parameter is verified. Analyzing Figures 8(a) and 8(b) leads to the similar results as in previous part. The correlation coefficient between the two sensitivity functions is 0.46. Thus, the two parameters can be identified. Note that between the two configurations, the magnitudes of θ and ψ are higher and lower for the second configuration, respectively. Those results is probably due to height reduced by two in the second case.

The parameter estimation problem is solved to retrieve the surface transfer coefficient. The algorithms are set with the same tolerances and discretisation parameters as previously. Figures 9(a) to 9(c) present the rate of convergence of the inverse problem algorithm. Compared to the previous case, it requires two times more iterations to reach the tolerance of 10^{-5}. The estimated parameters are $h_t^\circ = 129.4\ \mathsf{W.m^{-2}.K^{-1}}$

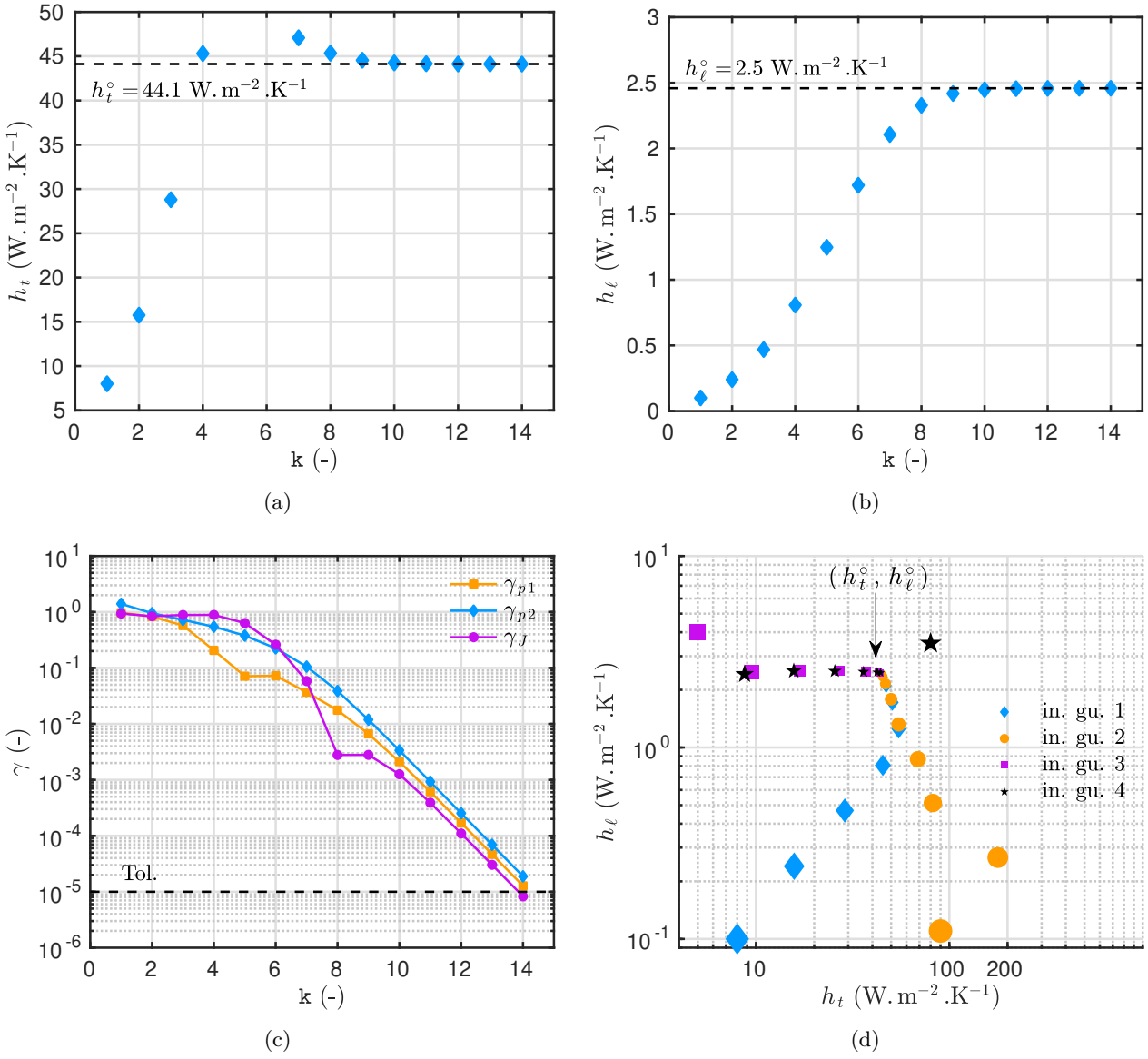

Figure 6. *Variation of the estimated surface transfer coefficients* h_t (a) *and* h_ℓ (b) *according to the iteration number. Variation of the convergence criteria of the inverse problem algorithm* (c). *Variation of the estimated surface transfer coefficients for four different initial guesses in the inverse problem algorithm* (d). *For the latter, the size of the marker decreases with the iteration number. Results corresponds to configuration 1.*

and $h_\ell^\circ = 4.5\,\mathrm{W.m^{-2}.K^{-1}}$, as reported in Table 1. The robustness of the solution is evaluated by running the inverse problem algorithm considering four different initial guesses. As shown in Figure 9(d), the same solution is obtained in the end.

Secondly, an equivalent configuration is defined with the proportionality ratio $\Pi = 5$. The corresponding dimensions of the material are presented in Table 1. With a proportionality ratio $\Pi > 1$, the characteristic time and lengths are increased compared to the experimental configuration. Particularly, the final time of the simulation is 125 h. The numerical prediction of the equivalent configuration are compared to the measurement of the experimental one in Figure 10. A good agreement is observed between both. Furthermore, the residual between both results remains in the range of the experimental uncertainties. Some slight discrepancies can be remarked in Figure 10(b) for $t^\star \in [0.5, 0.8]$. They arise probably from a missing phenomena in the description of the mathematical model. However, the overall results are very

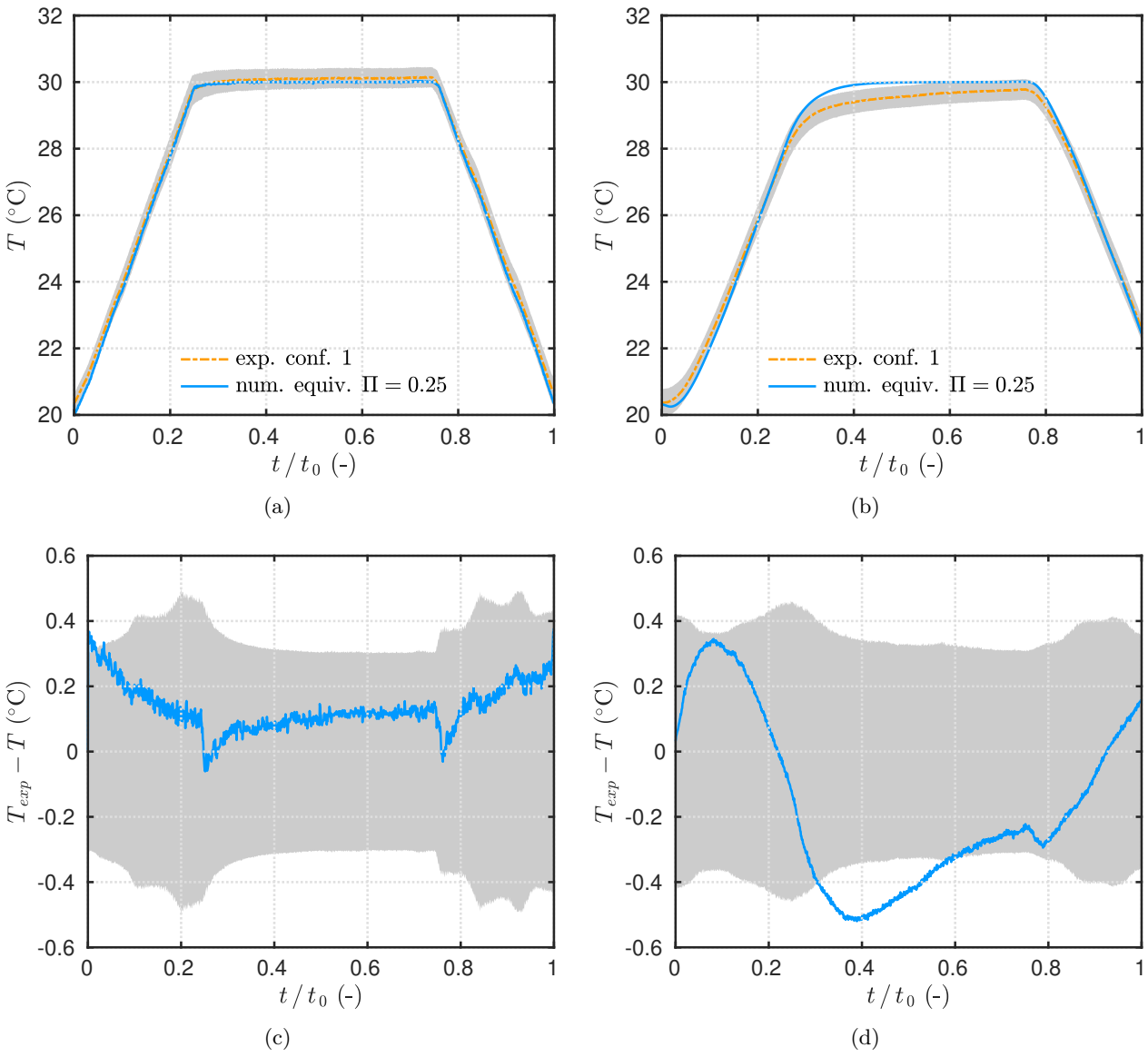

Figure 7. *Time variation of experimental results for configuration 1 and the model prediction for the equivalent configuration with* $\Pi = 0.25$ *for the first sensor* (x_1, y_1) (a) *and the second sensor* (x_2, y_2) (b). *Time variation of the residual between model predictions and experimental observations for the first sensor* (x_1, y_1) (c) *and the second sensor* (x_2, y_2) (d).

satisfying, highlighting a good reliability of the similarity law for the considered problem of heat transfer.

5.3 Complementary remarks

Regarding the computational time of the parameter estimation, each run of the direct problem scales with 40 s evaluated on a computer equipped with Intel Xeon(R) Gold (2.2 GHz 6^{th}) and 125.6 GB of RAM. The Gauß algorithm is selected to solve the parameter estimation problem for its fast convergence. Note that to verify that the inverse problem solution does not correspond to a local minimum, several runs are carried out with different initial parameters. With 15 to 30 iterations, the algorithm retrieves the unknown parameters, corresponding to a computational cost around 15 min. The use of probabilistic approaches to solve the inverse problem would face important computational issues. Bayesian or Particle Swarm algorithms require 10^3 to 10^4 computations of the direct problem to converge. To reduce this computational cost, reduced order model of the mathematical model should be required.

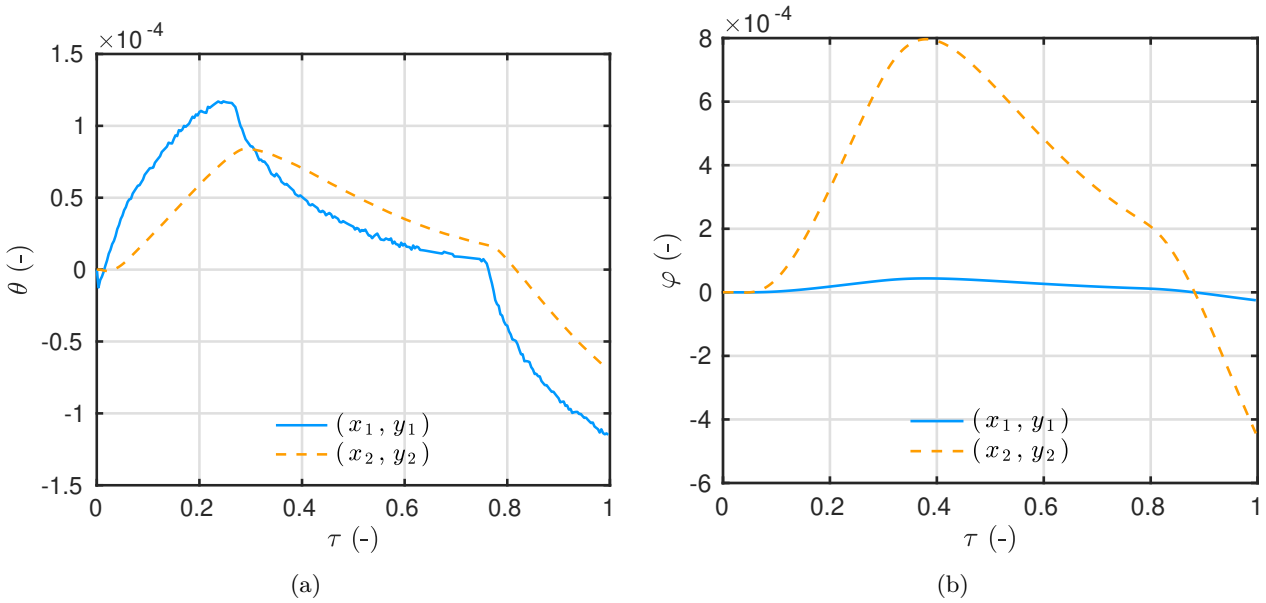

Figure 8. *Variation of the sensitivity function of the coefficients* h_t (a) *and* h_ℓ (b) *computed with the initial guesses.*

The experiment is assumed as two-dimensional based on the configuration. As illustrated in Figure 1, the material is inserted into an insulation foam. The lateral gaps height is increased in the illustration for the sake of clarity. In reality, it scales with $\mathcal{O}(3)$ mm. Those lateral gaps are large enough to allow heat transfer on boundaries Γ_L and Γ_R. And they are small enough to have a heat surface coefficient h_ℓ different from the top one h_t. Thus, the asymmetry on the lateral and top surface heat coefficients forces the two-dimensional heat transfer during the experiment. Complementary investigations are carried to evaluate the importance of the two-dimensional effect. Figure 11 compares the two modeling approaches, namely one and two-dimensional simulations. For both configurations, as expected, there is almost no changes on the top surface measurement. However, for the middle sensor, the discrepancies are higher. Particularly for configuration 1, the differences scales with 2 °C. It highlights the importance of two-dimensional transfer in the experiment.

The climate chamber do not enable the control of the relative humidity. However, the relative humidity $\phi\,[-]$ have been monitored with the sensors inside the material. As remarked in Figure 13(a), the humidity is almost constant in time around 0.3 for both configurations. The small oscillations remains in the lower hygroscopic state of the material. It can be assumed that the mass transfer are almost in steady state and do not influence the heat one. Furthermore, the thermal conductivity of wood fiver varies according to both temperature and relative humidity. However, in our investigations, only temperature variation is assumed. According to [9], the sorption curve of the material and thermal conductivity are given by:

$$\Theta(\phi) = 40\,\phi^3 - 49\,\phi^2 + 27.02\,\phi,$$
$$\widetilde{k}(T) = k(T) + k_2 \cdot \Theta,$$

where $\Theta\,[-]$ is the mass basis moisture content in the material, where $k(T)$ is the function for thermal conductivity given by Eq. (2) and $\widetilde{k}(T)$ the one considering the variation with moisture content. The coefficient is $k_2 = 0.28 \cdot 10^{-3}\ \mathrm{W.m^{-1}.K^{-1}}$. To evaluate the hypothesis neglecting the moisture content variation, the following relative error is defined:

$$\varepsilon_r \circ k \overset{\text{def}}{:=} \frac{k - \widetilde{k}}{\widetilde{k}},$$

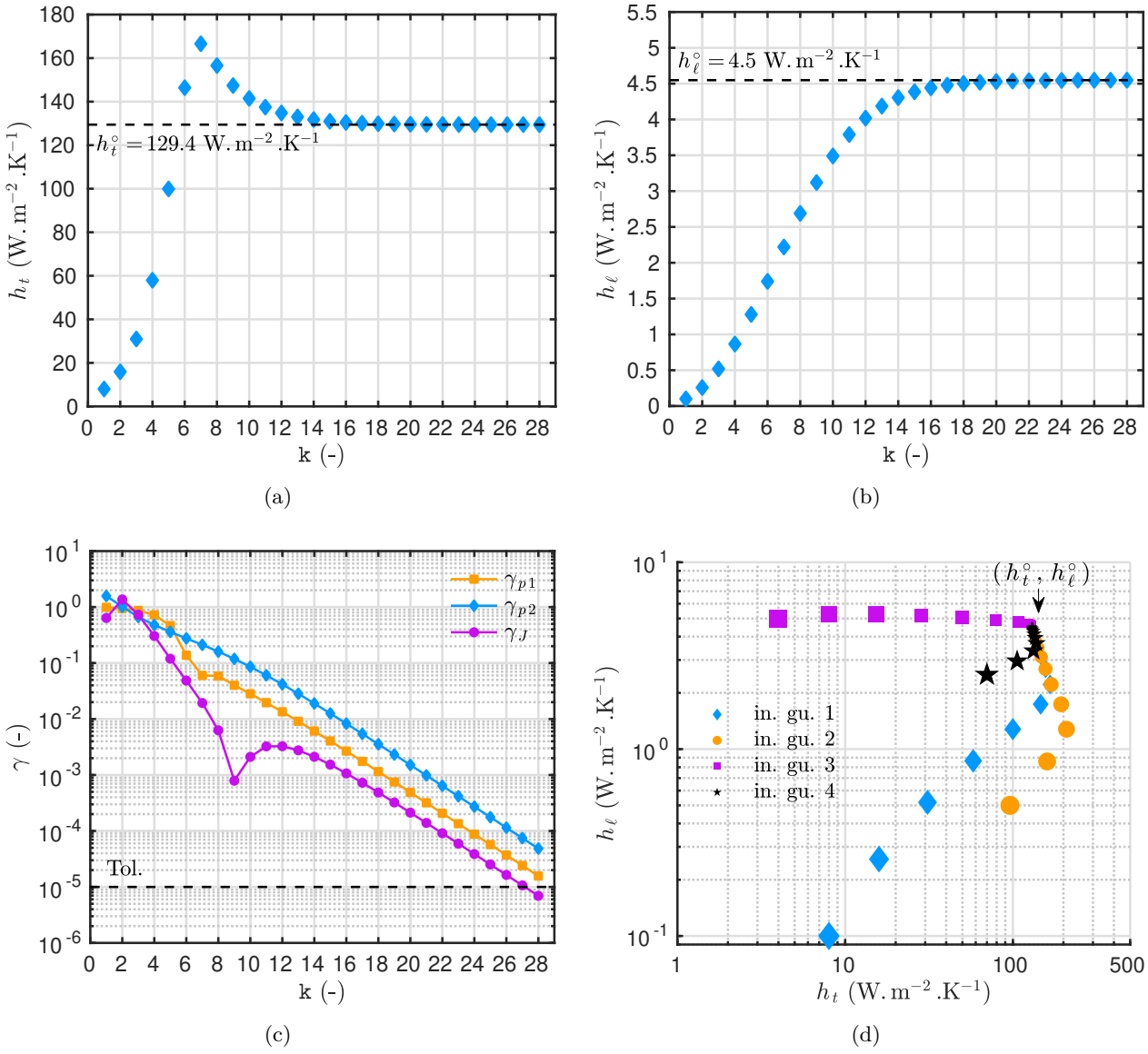

Figure 9. *Variation of the estimated surface transfer coefficients* h_t (a) *and* h_ℓ (b) *according to the iteration number. Variation of the convergence criteria of the inverse problem algorithm* (c). *Variation of the estimated surface transfer coefficients for four different initial guesses in the inverse problem algorithm* (d). *For the latter, the size of the marker decreases with the iteration number. Results correspond to configuration 2.*

computed using the measurement of temperature and relative humidity. The time variation of the relative error is given in Figure 13(b). The error is acceptable scaling with 3 %. Thus, the hypothesis of considering only temperature variation of the thermal conductivity is acceptable for the investigations.

The reliability of the similarity laws is discussed regarding the measurement uncertainties. The latter have been evaluated through a complete uncertainty propagation. In addition to the sensor measurement accuracy, the random part and the sensor position are also considered. The former is determined considering 3 sets of measurements carried for each campaign. The latter is retrieved through the space partial derivative of the temperature computed with a numerical model. The contribution of each uncertainty is shown in Figure 12 for both configurations. The uncertainty due to sensor position is higher during the transient state of the phenomena. It is consistent since it depends on the partial derivative $\frac{\partial T}{\partial x}$. It is higher for configuration 2 due to smaller material sample. The random part uncertainty scales with 0.2 °C and 0.1 °C

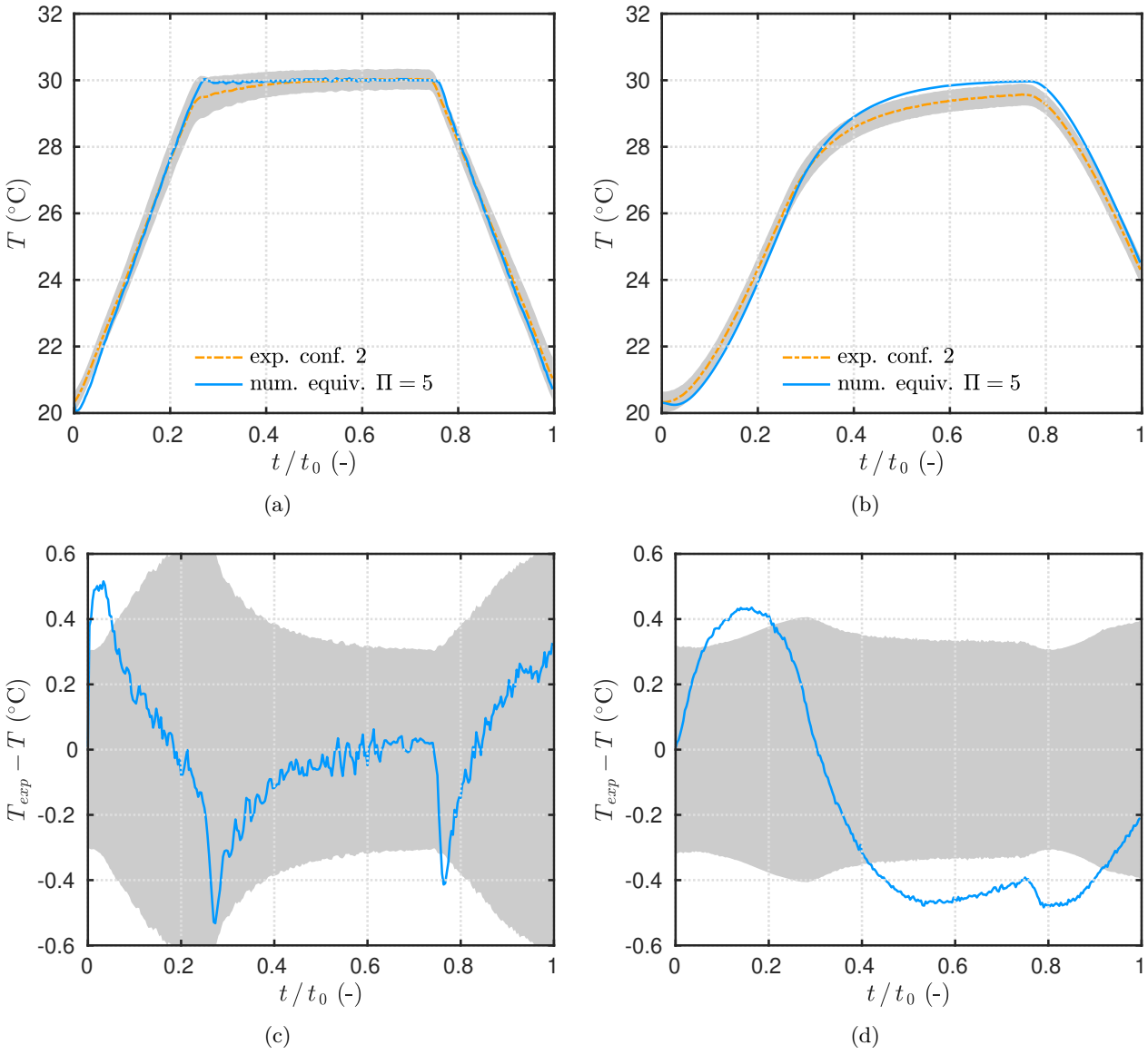

Figure 10. *Time variation of experimental results for configuration 2 and the model prediction for the equivalent configuration with* $\Pi = 5$ *for the first sensor* (x_1, y_1) (a) *and the second sensor* (x_2, y_2) (b). *Time variation of the residual between model predictions and experimental observations for the first sensor* (x_1, y_1) (c) *and the second sensor* (x_2, y_2) (d).

for configuration 1 and 2, respectively. The measurements among the three sets are more uncertain for configuration 1. Note that it is almost constant in time. Last, the sensor measurement uncertainty has the higher contribution among the three contributions.

It is important to remark that the similarity laws assumed that the material properties between two configurations have the same behavior. In other words, it is assumed that the function describing the thermal conductivity non-linearity does not change among the equivalent configurations. This assumption is certainly acceptable for wood fiber but requires further investigations for materials such as hemp concrete with complex micro-structures. For this reason, the extension of similarity laws for coupled heat and mass transfer in building porous material should be demonstrated.

Last, those investigations shows the reliability of similarity laws for two-dimensional heat transfer in building material. Those results may be important for the field. Indeed several similitude laws can be characterized for kinetic, geometric or transfer dynamics. Physically similar systems can be defined through

equivalent dimensionless numbers by changing the reference time or length of the material. Among several, two interesting examples can be illustrated. First, similarity laws can be used for insulation designs involving porous materials. For instance, equivalent geometric configurations of materials can be determined to achieve a certain given objective minimizing the heat losses. One could choose between two materials of different lengths $\overline{L}_0$ and $\widehat{L}_0$ to reach the same degree of insulation. Second example concerns experimental investigations. Some studies as material durability issues, require to be performed over a long time (several years). The similarity laws enable to changes the duration of the experiments by modifying the lengths and time scales of the material without modifying the dynamic of the heat transfer. In this way, faster equivalent experimental designs can be defined. An example of such assessment is proposed by Matsumoto and Fujiwara in [5]. The risk of condensation in a wall is assessed by investigating a reduced scale configuration.

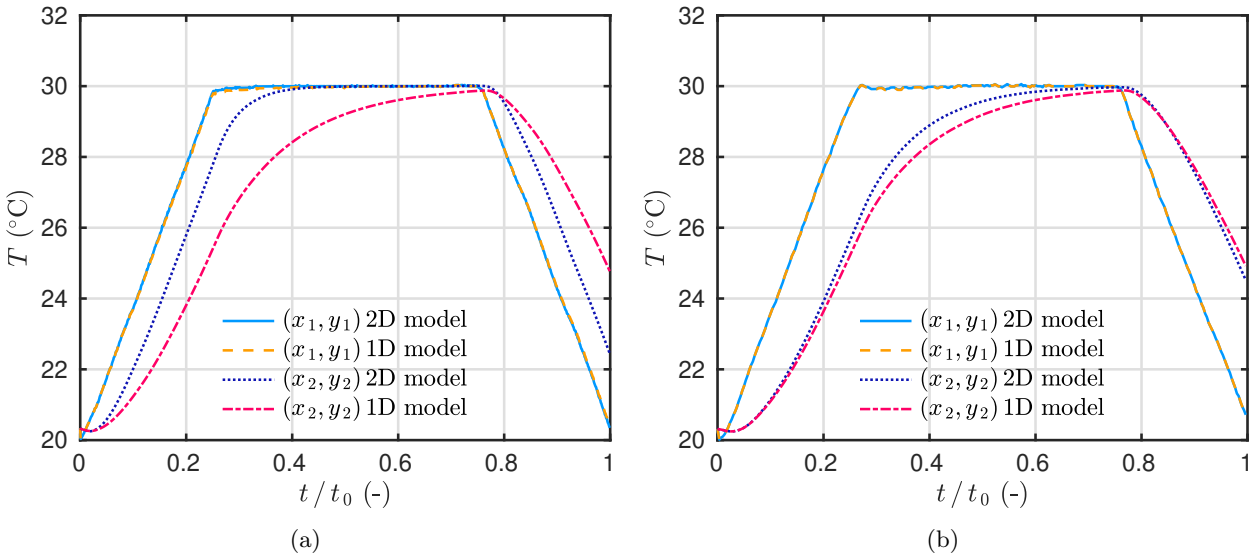

Figure 11. *Time variation of the predicted temperature with two-dimensional and one-dimensional models for configuration 1* (a) *and 2* (b)

6 Conclusion

This article evaluates the reliability of the similarity laws for a non-linear problem of two-dimensional heat transfer in a building porous material. For this, experimental observations are generated for two different configurations considering a wood fiber material submitted to a dynamic stress using a climatic chamber. The investigations lead to the following conclusions:

- A complete uncertainty propagation is carried out to evaluate the influence of the sensor measurement, of the random part and of the sensor position. The contribution of each uncertainty highlights that the sensor position mainly impacts during the transient state. The random part, evaluated using 3 sets of measurement, is almost constant in time. The sensor measurement has the higher contribution. The total uncertainty scales with 0.3 °C.
- A parameter estimation problem is solved to retrieve the two heat surface transfer coefficients. A Gauß algorithm is employed to determine with a low computational cost the top and lateral heat surface coefficients for both experimental configurations. Reliability of the estimates is verified by solving the inverse problem for various initial guesses in the algorithm. Results show that lateral heat surface coefficient is lower than top one since the latter is exposed to the direct airflow of the chamber ventilator.

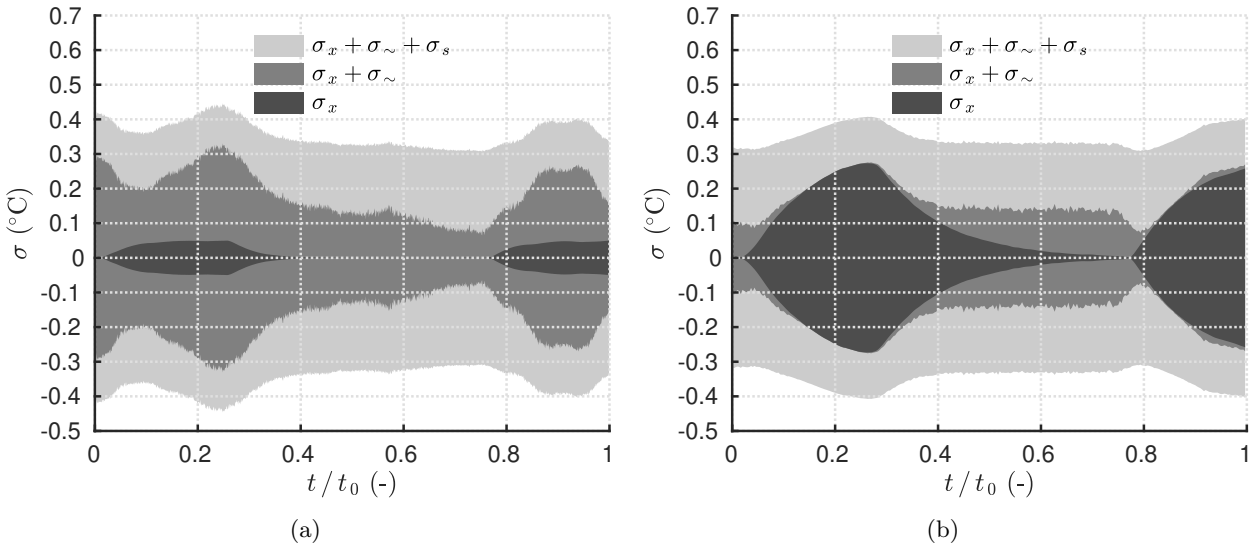

Figure 12. *Time variation of the temperature measurement in the material for configuration 1* (a) *and 2* (b)*.Time variation of the uncertainty contributions due to sensor position, random part and sensor measurement for configuration 1* (a) *and 2* (b)*.*

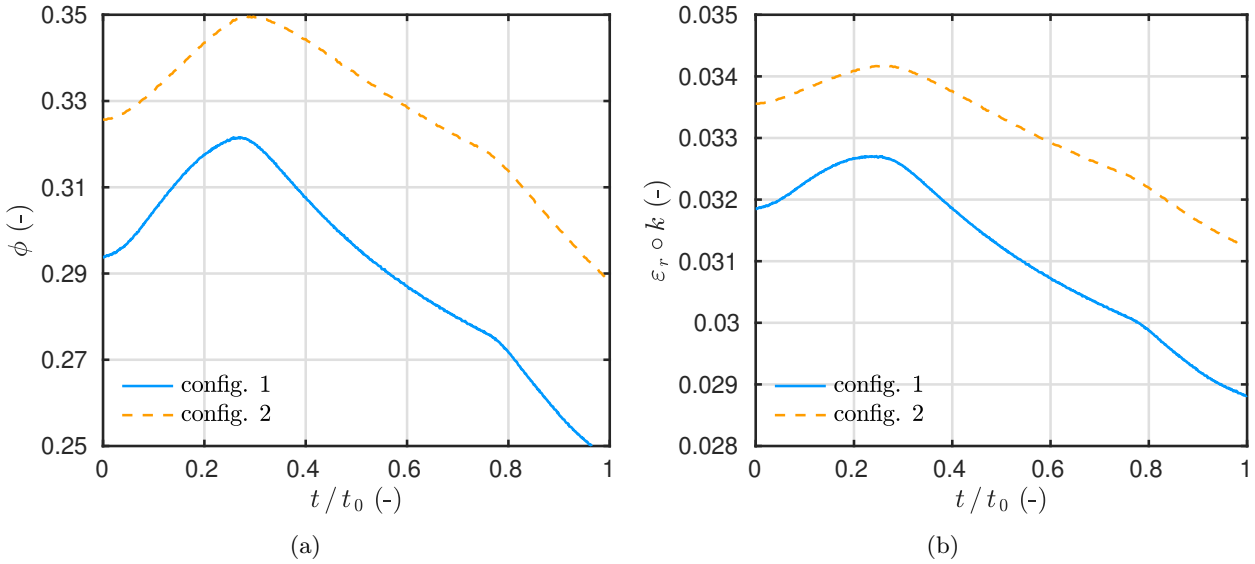

Figure 13. *Time variation of the measured relative humidity inside the material* (a) *and of the relative error on the thermal conductivity evaluated using measured temperature and relative humidity inside material* (b)*.*

- Once the coefficients known, the similarity laws of heat transfer are applied to define equivalent configurations. A comparison between the experimental observations and the numerical predictions for a equivalent configuration is performed. A very good agreement between both is remarked. The discrepancies remains in the range of the measurement uncertainties.
- The reliability of the similarity laws for defining equivalent configurations in terms of dynamics of nonlinear two-dimensional heat transfer in building porous materials is validated. Thus, several similitude laws can be defined for kinetic, geometric or transfer dynamics. Physically equivalent systems can be characterized enabling to achieve designs in terms of insulation or to reduce the duration of experiments to assess material durability issues for instance.

Further investigations should concern the reliability of similarity laws for coupled heat and mass transfer in building porous material. The material properties faces strong non-linearity that may lead to discrepancies in the experimental results.

Acknowledgments

The authors acknowledge the grants from the French Agency for Ecological Transition (ADEME).

Nomenclature and symbols

Physical parameters		
	Latin letters	
c	volumetric heat capacity	$\left[\mathsf{W.m^{-3}.K^{-1}}\right]$
h	heat transfer coefficient	$\left[\mathsf{W.m^{-2}.K^{-1}}\right]$
k , $\widetilde{k}$, k_0 , k_1 , k_2	thermal conductivity	$\left[\mathsf{W.m^{-1}.K^{-1}}\right]$
L	length	$\left[\mathsf{m}\right]$
N_e	number of experiment sets	$\left[-\right]$
N_s	number of sensors	$\left[-\right]$
N_m	number of time measurements	$\left[-\right]$
R	ambient temperature rate increase	$\left[\mathsf{^\circ C.s^{-1}}\right]$
T	temperature	$\left[\mathsf{K}\right]$
t , t_a , t_b	time	$\left[\mathsf{s}\right]$
x , y , z	coordinates	$\left[\mathsf{m}\right]$
	Greek letters	
ϕ	relative humidity	$\left[-\right]$
Θ	mass basis moisture content	$\left[-\right]$
σ	measurement uncertainty	$\left[\mathsf{K}\right]$
δ_x	sensor position uncertainty	$\left[\mathsf{m}\right]$

Mathematical notations	
	Latin letters
Bi	Biot number
Fo	Fourier number
`k`	Parameter estimation algorithm
r	length ratio
u	dimensionless temperature
$\mathcal{S}$	similarity laws application
Tol	Parameter estimation algorithm tolerance
	Greek letters
χ , ψ	dimensionless space coordinates
$\varepsilon_r \circ k$	relative error
κ	dimensionless conductivity
Γ	domain boundary
Ω	space or time domain
Π	proportionality factor of similarity laws
φ	sensitivity function relative to Bi_ℓ
τ	dimensionless time
θ	sensitivity function relative to Bi_t

Mathematical notations	
	Subscripts and superscripts
i	initial condition
exp	best estimate of measurement
obs	measurement
ℓ	lateral surface
t	top surface
T , B , L , R	top, bottom, left, right boundaries
x , y	relative to height and width, respectively
∞	ambient air
0	reference state
$\star$	dimensionless formulation
$\circ$	estimated parameter
$\sim$	random measurement
s	sensor measurement
χ	sensor position

A Parameter estimation problem

The issue is to determine the surface transfer coefficient h_ℓ and h_t, or their equivalent in terms of dimensionless parameters Bi_ℓ and Bi_t. For this, the unknown parameter p is defined by:

$$p \overset{\text{def}}{:=} (p_1, p_2) \;=\; (\mathrm{Bi}_t, \mathrm{Bi}_\ell)\,.$$

The row vector of parameters is:

$$\boldsymbol{P} \overset{\text{def}}{:=} \Big[\, p_1, p_2 \Big]\,.$$

A.1 Gauß Algorithm

The estimate parameter verifies:

$$\boldsymbol{p}^\circ \;=\; \arg\min J(\boldsymbol{p})\,,$$

where J is the least square estimator formulated through a matrix formulation:

$$J \;=\; (\boldsymbol{U}_{\text{exp}} \;-\; \boldsymbol{U})\, W\, (\boldsymbol{U}^t_{\text{exp}} \;-\; \boldsymbol{U}^t)\,,$$

where $\boldsymbol{U}_{\text{exp}}$ is the row vector of experimental observations:

$$\boldsymbol{U}_{\text{exp}} \overset{\text{def}}{:=} \Big[\boldsymbol{U}^1_{\text{exp}}, \ldots, \boldsymbol{U}^{N_s}_{\text{exp}}\Big]\,, \qquad \boldsymbol{U}^i_{\text{exp}} \overset{\text{def}}{:=} \Big[u_{\text{exp}}(x_i, y_i, t^1), \ldots, u_{\text{exp}}(x_i, y_i, t^{N_m})\Big]\,,$$

recalling that N_s and N_m are the number of sensors and time measurement, respectively. The quantity u_{exp} is obtained by the experimental campaign. The row vector $\boldsymbol{U}$ of direct model predictions is:

$$\boldsymbol{U} \overset{\text{def}}{:=} \Big[\boldsymbol{U}^1, \ldots, \boldsymbol{U}^{N_s}\Big]\,, \qquad \boldsymbol{U}^i \overset{\text{def}}{:=} \Big[u(x_i, y_i, t^1), \ldots, u(x_i, y_i, t^{N_m})\Big]\,,$$

where u arises from the computation of the so-called direct problem, defined by Eqs. (6), (8), and (10). It is computed using a candidate parameter $\boldsymbol{p}$. Last, $W \;=\; \sigma^{-2}\boldsymbol{I}$ is the inverse covariance matrix of measurement uncertainties.

To minimize the cost function J, the Gauß algorithm is used. Starting from a parameter $\boldsymbol{P}^k$, a new (better) candidate parameter is obtained by:

$$\boldsymbol{P}^{k+1} \;=\; \boldsymbol{P}^k \;+\; \Delta^k_{\boldsymbol{p}}\,, \tag{13}$$

with $\Delta^k_{\boldsymbol{p}}$ the parameter increment vector obtained by:

$$\Delta^k_{\boldsymbol{p}} \overset{\text{def}}{:=} (\boldsymbol{X}\,\boldsymbol{W}\,\boldsymbol{X}^t)^{-1} \left(\boldsymbol{X}\,\boldsymbol{W}\,(\boldsymbol{U}^t \;-\; \widehat{\boldsymbol{U}}^t)\right),$$

where $\boldsymbol{X}$ is the sensitivity matrix according to parameters evaluated using $\boldsymbol{P}^k$. The later is defined by:

$$\boldsymbol{X} \overset{\text{def}}{:=} \Big[\boldsymbol{X}^1, \ldots, \boldsymbol{X}^{N_s}\Big]\,, \qquad \boldsymbol{X}^i \overset{\text{def}}{:=} \begin{bmatrix} \dfrac{\partial u}{\partial p_1}(x_i, y_i, t^1), \ldots, \dfrac{\partial u}{\partial p_1}(x_i, y_i, t^{N_m}) \\ \dfrac{\partial u}{\partial p_2}(x_i, y_i, t^1), \ldots, \dfrac{\partial u}{\partial p_2}(x_i, y_i, t^{N_m}) \end{bmatrix}, \tag{14}$$

with the sensitivity functions $\dfrac{\partial u}{\partial p_1}$ and $\dfrac{\partial u}{\partial p_2}$ computed by direct differentiation of the equations as described in the next Section.

The algorithm iterates over the index $\mathtt{k}$ until one of the three criteria is met:

$$\gamma_{p,j} \leqslant \mathrm{Tol}_1\,, \quad \forall j \in \{1, 2\}\,, \quad \gamma_2 \leqslant \mathrm{Tol}_2\,, \quad \mathtt{k} \geqslant N_k\,,$$

where

$$\gamma_{p,j} \overset{\text{def}}{:=} \frac{\left\| p^{k+1}_j \;-\; p^k_j \right\|_2}{\left\| p^k_j \right\|_2}\,, \qquad \gamma_2 \overset{\text{def}}{:=} \frac{\left\| J(\boldsymbol{p}^{k+1}) \;-\; J(\boldsymbol{p}^k) \right\|_2}{\left\| J(\boldsymbol{p}^k) \right\|_2}\,. \tag{15}$$

Algorithm 1 synthesizes the main steps of the method.

Algorithm 1 Gauß parameter estimation algorithm.

1: Set iteration indicator $\mathtt{k} \;=\; 1$
2: **while** $\gamma_{p\,,\,j} \;\geqslant\; \mathrm{Tol}_1 \quad \& \quad \gamma_2 \;\geqslant\; \mathrm{Tol}_2 \quad \& \quad k \;\leqslant\; N_k$ **do**
3: Compute the direct model $\boldsymbol{U}$ and sensitivity matrix $\boldsymbol{X}$
4: Compute the cost function $\boldsymbol{J}$
5: Found new candidate of estimate $\boldsymbol{P}^{\,k+1}$ from Eq. (13)
6: Compute stopping criteria $\gamma_{p\,,\,j}$ and γ_2 from Eq. (15)
7: $\mathtt{k} \;=\; \mathtt{k} + 1$
8: **end**

A.2 Sensitivity equations

To compute the sensitivity matrix $\boldsymbol{X}$ from Eq. (14), the sensitivity functions $\dfrac{\partial u}{\partial p_1}$ and $\dfrac{\partial u}{\partial p_2}$ need to be evaluated. For the sake of clarity, the functions are denoted by:

$$\theta \;\overset{\text{def}}{\coloneqq}\; \frac{\partial u}{\partial \mathrm{Bi}_t} \;=\; \frac{\partial u}{\partial p_1}\,, \qquad \varphi \;\overset{\text{def}}{\coloneqq}\; \frac{\partial u}{\partial \mathrm{Bi}_\ell} \;=\; \frac{\partial u}{\partial p_2}\,,$$

Both are obtained by direct differentiation of the governing equations Eqs. (6), (8), and (10). Thus, θ is given by equation:

$$\frac{\partial \theta}{\partial \tau} \;= \mathrm{Fo}\cdot\frac{\partial}{\partial \chi}\left(\kappa(u)\cdot\frac{\partial \theta}{\partial \chi}\right) \;+\; \mathrm{Fo}\cdot r^{\,2}\cdot\frac{\partial}{\partial \psi}\left(\kappa(u)\cdot\frac{\partial \theta}{\partial \psi}\right) \tag{16}$$

$$+\;\mathrm{Fo}\cdot\frac{\partial}{\partial \chi}\left(\kappa'(\theta)\cdot\frac{\partial u}{\partial \chi}\right) \;+\; \mathrm{Fo}\cdot r^{\,2}\cdot\frac{\partial}{\partial \psi}\left(\kappa'(\theta)\cdot\frac{\partial u}{\partial \psi}\right), \tag{17}$$

where $\kappa'(\theta) \;=\; \kappa_1\cdot\theta$. It is completed with the following boundary conditions:

$$\begin{aligned}
\kappa(u)\cdot\frac{\partial \theta}{\partial \chi} \;&=\; \mathrm{Bi}_t\cdot\theta \;+\; \Big(u \;-\; u_\infty(\tau)\Big) \;-\; \kappa'(\theta)\cdot\frac{\partial u}{\partial \chi}\,, && \forall(\chi\,,\,\psi) \;\in\; \Gamma^\star_T\,,\\
\frac{\partial \theta}{\partial \chi} \;&=\; 0\,, && \forall(\chi\,,\,\psi) \;\in\; \Gamma^\star_B\,,\\
\kappa(u)\cdot\frac{\partial \theta}{\partial \psi} \;&=\; \mathrm{Bi}_\ell\cdot r\cdot\theta \;-\; \kappa'(\theta)\cdot\frac{\partial u}{\partial \chi}\,, && \forall(\chi\,,\,\psi) \;\in\; \Gamma^\star_L\,,\\
\kappa(u)\cdot\frac{\partial \theta}{\partial \psi} \;&=\; -\,\mathrm{Bi}_\ell\cdot r\cdot\theta \;-\; \kappa'(\theta)\cdot\frac{\partial u}{\partial \chi}\,, && \forall(\chi\,,\,\psi) \;\in\; \Gamma^\star_R\,,
\end{aligned}$$

and the initial condition

$$\theta \;=\; 0\,, \qquad \forall(\chi\,,\,\psi) \;\in\; \big[\,0\,,\,1\,\big]^{\,2}\,, \qquad \tau \;=\; 0\,.$$

Similarly, the sensitivity function φ verifies the equation:

$$\frac{\partial \varphi}{\partial \tau} \;= \mathrm{Fo}\cdot\frac{\partial}{\partial \chi}\left(\kappa(u)\cdot\frac{\partial \varphi}{\partial \chi}\right) \;+\; \mathrm{Fo}\cdot r^{\,2}\cdot\frac{\partial}{\partial \psi}\left(\kappa(u)\cdot\frac{\partial \varphi}{\partial \psi}\right) \tag{18}$$

$$+\;\mathrm{Fo}\cdot\frac{\partial}{\partial \chi}\left(\kappa'(\varphi)\cdot\frac{\partial u}{\partial \chi}\right) \;+\; \mathrm{Fo}\cdot r^{\,2}\cdot\frac{\partial}{\partial \psi}\left(\kappa'(\varphi)\cdot\frac{\partial u}{\partial \psi}\right), \tag{19}$$

where $\kappa'(\varphi) = \kappa_1 \cdot \varphi$. The boundary conditions are:

$$\begin{aligned}
\kappa(u)\cdot\frac{\partial\varphi}{\partial\chi} &= \mathrm{Bi}_t\cdot\varphi - \kappa'(\varphi)\cdot\frac{\partial u}{\partial\chi}, && \forall(\chi,\psi)\in\Gamma_T^\star,\\
\frac{\partial\varphi}{\partial\chi} &= 0, && \forall(\chi,\psi)\in\Gamma_B^\star,\\
\kappa(u)\cdot\frac{\partial\varphi}{\partial\psi} &= \mathrm{Bi}_\ell\cdot r\cdot\varphi + \Big(u - u_\infty(\tau)\Big) - \kappa'(\varphi)\cdot\frac{\partial u}{\partial\chi}, && \forall(\chi,\psi)\in\Gamma_L^\star,\\
\kappa(u)\cdot\frac{\partial\varphi}{\partial\psi} &= -\mathrm{Bi}_\ell\cdot r\cdot\varphi - \Big(u - u_\infty(\tau)\Big) - \kappa'(\varphi)\cdot\frac{\partial u}{\partial\chi}, && \forall(\chi,\psi)\in\Gamma_R^\star,
\end{aligned}$$

and the initial condition are

$$\varphi = 0, \qquad \forall(\chi,\psi)\in\big[0,1\big]^2, \qquad \tau = 0.$$

B Du Fort–Frankel Numerical model

This Section describes the computation of the direct problem to obtain the field u and the sensitivity functions θ and ψ. A finite–differences approach is considered with a uniform discretisation for space and time lines. More precisely, the Du Fort–Frankel scheme is employed to build an efficient numerical model for the two-dimensional heat diffusion equation. It offers an explicit formulation with a relaxed boundary conditions as demonstrated in [11]. Here, compared to [11], the scheme is extended to an equation with a time-dependent source term and non-linear diffusion properties.

One can note that Eqs. (6), (16) and (18) are very similar from a point of view of partial differential equations. Thus, for the sake of simplicity, the numerical scheme is presented for the following equation:

$$\frac{\partial v}{\partial t} = \frac{\partial}{\partial x}\Big(k_x(v)\cdot\frac{\partial v}{\partial x}\Big) + \frac{\partial}{\partial y}\Big(k_y(v)\cdot\frac{\partial v}{\partial y}\Big) + S(x,y,t),$$

where v stands for u, θ or φ. The discrete values of the function $v(x,y,t)$ are written as $v_{ji}^n \overset{\text{def}}{:=} u(x_j, y_i, t^n)$ with $i = \{1,\dots,N_y\}$, $j = \{1,\dots,N_x\}$ and $n = \{1,\dots,N_t\}$. The quantities N_x, N_y and N_t are the numbers of nodes for x, y and t coordinates, respectively. The discretisation parameters are denoted using Δt for the time, Δx for the x space and Δy for the y one. Following the demonstration provided in [11], the Du Fort–Frankel scheme yields to the following explicit expression:

$$\begin{aligned}
v_{ji}^{n+1} &= \Sigma_x\cdot\Big(k_x^-\cdot v_{j-1\,i}^n + k_x^+\cdot v_{j+1\,i}^n\Big) + \Sigma_y\cdot\Big(k_y^-\cdot v_{ji-1}^n + k_y^+\cdot v_{ji+1}^n\Big)\\
&\quad + \Sigma_{xy}\cdot v_{ji}^{n-1} + \Sigma_s\cdot S_{ji}^n,
\end{aligned}$$

where the coefficients are given by:

$$\begin{aligned}
\Sigma_x &\overset{\text{def}}{:=} \frac{\lambda_x}{1+\lambda_x\cdot k_x^\circ+\lambda_y\cdot k_y^\circ}, & \Sigma_y &\overset{\text{def}}{:=} \frac{\lambda_y}{1+\lambda_x\cdot k_x^\circ+\lambda_y\cdot k_y^\circ},\\
\Sigma_{xy} &\overset{\text{def}}{:=} \frac{1-\lambda_x\cdot k_x^\circ-\lambda_y\cdot k_y^\circ}{1+\lambda_x\cdot k_x^\circ+\lambda_y\cdot k_y^\circ}, & \Sigma_s &\overset{\text{def}}{:=} \frac{2\cdot\Delta t}{1+\lambda_x\cdot k_x^\circ+\lambda_y\cdot k_y^\circ},\\
\lambda_x &\overset{\text{def}}{:=} \frac{2\,\Delta t}{\Delta x^2}, & \lambda_y &\overset{\text{def}}{:=} \frac{2\,\Delta t}{\Delta y^2},
\end{aligned}$$

and the nonlinear properties coefficients are defined by:

$$\begin{aligned}
k_x^+ &\overset{\text{def}}{:=} k_x\Big(v_{j+\frac12\,i}^n\Big), \quad k_x^- \overset{\text{def}}{:=} k_x\Big(v_{j-\frac12\,i}^n\Big), \quad k_x^\circ \overset{\text{def}}{:=} \frac12\Big(k_x^+ + k_x^-\Big),\\
k_y^+ &\overset{\text{def}}{:=} k_y\Big(v_{ji+\frac12}^n\Big), \quad k_y^- \overset{\text{def}}{:=} k_y\Big(v_{ji-\frac12}^n\Big), \quad k_y^\circ \overset{\text{def}}{:=} \frac12\Big(k_y^+ + k_y^-\Big),
\end{aligned}$$

with

$$v^{n}_{j\pm\frac{1}{2}\,i} \;=\; \frac{1}{2}\Big(\,v^{n}_{j\pm1\,i} \;+\; v^{n}_{j\,i}\,\Big)\,, \qquad v^{n}_{j\,i\pm\frac{1}{2}} \;=\; \frac{1}{2}\Big(\,v^{n}_{j\,i\pm1} \;+\; v^{n}_{j\,i}\,\Big)\,.$$

In addition, the boundary conditions are discretized using a second-order approach required to maintain the stability of the numerical scheme.

References

[1] N. Mendes, M. Chhay, J. Berger, and D. Dutykh. *Numerical Methods for Diffusion Phenomena in Building Physics: A Practical Introduction*. Springer International Publishing, 2019. 1

[2] T. Busser, J. Berger, A. Piot, M. Pailha, and M. Woloszyn. Comparison of model numerical predictions of heat and moisture transfer in porous media with experimental observations at material and wall scales: An analysis of recent trends. *Drying Technology*, 37(11):1363–1395, 2019. 1

[3] H. Rafidiarison, R. Rémond, and E. Mougel. Dataset for validating 1-D heat and mass transfer models within building walls with hygroscopic materials. *Building and Environment*, 89:356–368, 2015. 1

[4] A. Machard, C. Inard, J.M. Alessandrini, C. Pelé, and J. Ribéron. A Methodology for Assembling Future Weather Files Including Heatwaves for Building Thermal Simulations from the European Coordinated Regional Downscaling Experiment (EURO-CORDEX) Climate Data. *Energies*, 13(13):3424, 2020. 1

[5] M. Matsumoto and S. Fujiwara. A study of annual moisture variation in an internally insulated building wall under a mild climate using a small-scale model and the similarity laws. *Energy and Buildings*, 16(3):933–945, 1991. 1, 2, 15

[6] M. C. Ruzicka. On dimensionless numbers. *Chemical Engineering Research and Design*, 86(8):835–868, 2008. 1

[7] A. Trabelsi, Z. Slimani, and J. Virgone. Response surface analysis of the dimensionless heat and mass transfer parameters of Medium Density Fiberboard. *International Journal of Heat and Mass Transfer*, 127:623–630, 2018. 1

[8] J. Berger, C. Legros, and M. Abdykarim. Dimensionless formulation and similarity to assess the main phenomena of heat and mass transfer in building porous material. *Journal of Building Engineering*, 35:101849, 2021. 2

[9] T. Busser, J. Berger, A. Piot, M. Pailha, and M. Woloszyn. Dynamic experimental method for identification of hygric parameters of a hygroscopic material. *Building and Environment*, 131:197–209, 2018. 6, 12

[10] John R. Taylor and William Thompson. An Introduction to Error Analysis: The Study of Uncertainties in Physical Measurements. *Physics Today*, 51(1):57, January 2008. 7

[11] J. Berger, S. Gasparin, W. Mazuroski, and N. Mendes. An efficient two-dimensional heat transfer model for building envelopes. *Numerical Heat Transfer, Part A: Applications*, 79(3):163–194, 2021. 22